Moving gating charges through the gating pore in a Kv channel voltage sensor

Jérôme J. Lacroix[1], H. Clark Hyde[1], Fabiana V. Campos, and Francisco Bezanilla[2]

Department of Biochemistry and Molecular Biology, University of Chicago, Chicago, IL 60637

Contributed by Francisco Bezanilla, April 5, 2014 (sent for review January 29, 2014)

Voltage sensor domains (VSDs) regulate ion channels and enzymes by transporting electrically charged residues across a hydrophobic VSD constriction called the gating pore or hydrophobic plug. How the gating pore controls the gating charge movement presently remains debated. Here, using saturation mutagenesis and detailed analysis of gating currents from gating pore mutations in the Shaker Kv channel, we identified statistically highly significant correlations between VSD function and physicochemical properties of gating pore residues. A necessary small residue at position S240 in S1 creates a "steric gap" that enables an intracellular access pathway for the transport of the S4 Arg residues. In addition, the stabilization of the depolarized VSD conformation, a hallmark for most Kv channels, requires large side chains at positions F290 in S2 and F244 in S1 acting as "molecular clamps," and a hydrophobic side chain at position I237 in S1 acting as a local intracellular hydrophobic barrier. Finally, both size and hydrophobicity of I287 are important to control the main VSD energy barrier underlying transitions between resting and active states. Taken together, our study emphasizes the contribution of several gating pore residues to catalyze the gating charge transfer. This work paves the way toward understanding physicochemical principles underlying conformational dynamics in voltage sensors.

energy landscape | kinetic model | global fit

Membrane proteins controlled by the membrane potential are ubiquitous among phyla and are involved in a variety of fundamental biological tasks such as action potential generation and propagation, pacemaker activity, insulin secretion, G proteins and lipid signaling, innate immunity, and cell homeostasis (1–8). In most of these proteins, voltage sensitivity is conferred by small structural modules called voltage sensor domains (VSDs) that encompass four transmembrane helices S1–S4 (9). To date, VSDs have been identified in K^+, Na^+, Ca^{2+}, and H^+ channels, and in phosphoinositide phosphatases (2, 10, 11).

VSDs switch between several conformations depending on the membrane potential by virtue of positively charged residues, mostly Arg or Lys tethered to the S4 transmembrane helix, rearranging within the membrane electric field (12, 13). Although the transport of ionized groups through the cell membrane is thermodynamically unfavorable, their transfer is catalyzed in the VSD by the presence of negative counter charges in the S1–S3 segments and water-filled cavities that focus the electric field across a narrow 5- to 10-Å constriction termed the "gating pore," or "hydrophobic plug" (14–21), positioned at the midlevel of the membrane. Despite its narrow depth, the gating pore effectively insulates the two sides of the lipid bilayer and excludes the permeation of free ions. Voltage-gated proton channels are an exception, wherein the hydrophobic plug gates a proton permeation pathway (10, 11, 22).

Studies of depolarized X-ray structures of the K^+ channel Kv1.2 and of the Kv1.2/2.1 paddle chimera suggest that the gating pore is formed by 10 side chains, mostly hydrophobic, belonging to residues from the S1–S3 segments (Fig. 1 *A* and *B*) (21, 23). Investigations of the VSD hyperpolarized (resting) states using molecular dynamics simulations revealed that the gating pore remains formed by the same cluster of residues upon VSD rearrangements (Fig. S1) (6, 24–27).

In the human Kv1.1 channel, the inherited mutations I177N, F184C, and I262T, homologous to gating pore residues I237, F244, and I320 in the related Shaker Kv channel, are associated with type I episodic ataxia (28–31). Similarly, in the related VSD of human voltage-gated sodium channels, the inherited gating pore mutations I739V in Nav1.7, I141V in Nav1.4, F1250L in Nav1.5, and V1611F and V1612I in Nav1.1 (respectively homologous to residues I237, I241, F290, A319, and I320 in Shaker) are linked to Dravet syndrome (I739V, V1611F, and V1612I), paramyotonia congenita (I141V), and long QT syndrome (F1250L) (32–37) (Fig. 1*B*). These disease-associated mutations underscore the biological importance of the gating pore to regulate the voltage sensors in Kv and Nav channels.

Functional interactions between the gating charges and some gating pore residues have been identified (17, 38), but a complete description of this intramolecular gating network is lacking, as well as the nature of these interactions and their contributions to the energy profile underlying VSD transitions. Toward this goal, large-scale mutagenesis scanning has been useful to dissect structural and functional information in voltage-gated ion channels (39–45). However, although insightful to pinpoint functionally important residues, this approach struggled to identify precise physicochemical mechanisms because the endogenous residues were generally mutated by only one type of amino acid, often Ala or Trp.

Here, we characterized the effects of a large number of substitutions (12–15) in the gating pore of the Shaker K^+ channel, a prototypical Kv channel homolog to Kv1.2 (Fig. 1*B*). This approach led us to uncover nonambiguous quantitative correlations between the mutant phenotypes and specific physicochemical

Significance

Voltage sensors are integral membrane protein domains that regulate ion channels and enzymes by transporting electrically charged residues across a narrow constriction that focuses the membrane electrical field. Here, we investigated how this constriction, also called the "gating pore," controls this transport by studying the effects of a large number of point mutations. Our analysis indicates the presence of nonambiguous statistical correlations between specific amino acid lateral-chain physicochemical properties (size, hydrophobicity) and specific functional features of the voltage sensor (voltage sensitivity and transport kinetics). This study allowed us to propose engineering-like mechanisms by which gating pore residues control the voltage sensor operation.

Author contributions: J.J.L. and F.B. designed research; J.J.L. and F.V.C. performed research; H.C.H. and F.B. contributed new reagents/analytic tools; J.J.L., H.C.H., and F.B. analyzed data; and J.J.L., H.C.H., and F.B. wrote the paper.

The authors declare no conflict of interest.

Freely available online through the PNAS open access option.

[1]J.J.L. and H.C.H. contributed equally to this work.

[2]To whom correspondence should be addressed. E-mail: fbezanilla@uchicago.edu.

This article contains supporting information online at www.pnas.org/lookup/suppl/doi:10.1073/pnas.1406161111/-/DCSupplemental.

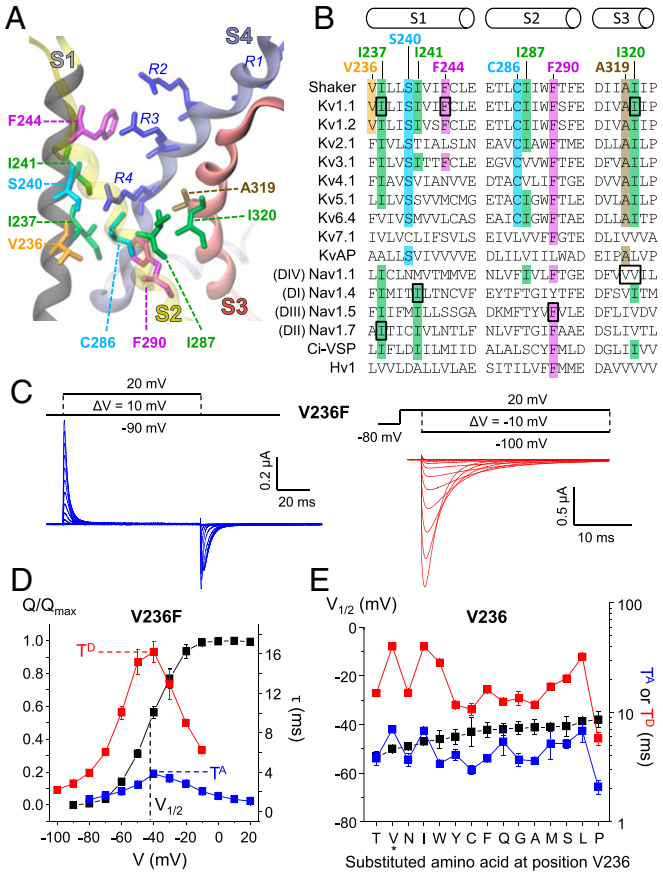

Fig. 1. The Kv channel gating pore and mutants characterization. (*A*) Refined X-ray structure of the Kv1.2 VSD (21) showing the S1–S4 helices, the gating charges R1–R4 (blue, licorice representation), and 10 gating pore residues in licorice representation: V236 (orange), I237 (green), S240 (cyan), I241 (green), and F244 (purple) in S1; C286 (cyan), I287 (green), and F290 (purple) in S2; A319 (brown) and I320 (green) in S3. Residue numbering is from Shaker. (*B*) Sequence alignment (T-Coffee) of gating pore residues in several VSDs (Shaker, GI: 13432103; Kv1.1, GI: 223590092; Kv1.2, GI: 4826782; Kv2.1, GI: 4826784; Kv3.1, GI: 76825377; Kv4.1, GI: 27436981; Kv5.1, GI: 24418476; Kv6.4, GI: 26006803; Kv7.1, GI: 32479527; KvAP, GI: 38605092; Nav1.1^{DIV}, GI: 12644229; Nav1.4^{DI}, GI: 292495096; Nav1.5^{DIII}, GI: 215273881; Nav1.7^{DII}, GI: 327478559; Ci-VSP, GI: 76253898; and Hv1, GI: 74751810). Coloring method is identical to *A*. Boxed residues indicate the position of mutations linked to human diseases. (*C*) Activation (blue; *Left*) and deactivation (red; *Right*) gating current recordings for V236F. (*D*) Activation (blue) and deactivation (red) gating current kinetics and relative charge *Q* (black) are plotted as a function of the pulse voltage (*V*) for V236F. T^A and T^D represent the slowest time constant for activation and deactivation, respectively, whereas $V_{1/2}$ represents the midpoint voltage of the *Q*–*V* curve. (*E*) The gating parameters T^A, T^D, and $V_{1/2}$ are plotted as a function of the side chain present at position V236, where amino acids are ordered according to a monotonic increase of the $V_{1/2}$ value. The native residue is indicated by an asterisk.

attributes of the substituted side chains. Because the gating pore residues are mostly hydrophobic across the tree of life, it is generally accepted that their hydrophobicity plays a major role in controlling VSD movement (17, 21, 38). However, we found that a hydrophobic side chain is only exclusively required for I237, whereas the size of the lateral chain is the critical parameter for S240, F244, and F290. These correlations allowed us to propose mechanistic contributions for several gating pore residues.

Results and Discussion

Functional Characterization of Gating Pore Mutations. Eight out of 10 residues forming the gating pore in the Shaker Kv channel (V236, I237, S240, F244, C286, I287, A319, and I320) (Fig. 1 *A* and *B*) were individually mutated by a large number of amino acids, creating an exhaustive library of 114 point mutations [see Table 1, which also includes previously reported mutations of I241, I287, and F290 (38, 46, 47)]. Each mutant was heterologously expressed in *Xenopus* oocytes and characterized using the high-resolution cut-open voltage-clamp technique (48). No gating currents could be detected in 15 out of 114 mutants (minus signs "–" in Table 1). Among them, the homologous mutations I237R, S240L, S240P, and S240R in the related potassium channel Kv1.1 were previously shown to abolish K^+ conduction (49).

Gating currents produced during the resting-to-active (activation) and active-to-resting (deactivation) transitions were recorded in the 99 functional mutants by blocking K^+ conduction using the mutation W434F, which favors a nonconducting (inactivated) state of the channel's pore (50–52). Activation gating currents were elicited by using depolarizing pulses (Fig. 1*C*, *Left*). Deactivation gating currents were elicited by using depolarizing prepulses of large amplitude to saturate the gating charge (*Q*) (Fig. 1*C*, *Right*). The duration of these activating prepulses was maintained as short as possible, albeit long enough to saturate the gating charge, to minimize the influence of VSD relaxation on the deactivation gating current kinetics (53).

For each mutant, we determined the time constant τ of activating and deactivating gating currents for all tested potentials and determined the corresponding bell-shaped τ vs. voltage (*V*) (τ–*V*) curves during activation and deactivation (*Materials and Methods*). We also determined the charge vs. voltage (*Q*–*V*) curves by integrating the activating gating currents over the pulse duration. Most *Q*–*V* curves exhibited a monotonic quasisigmoid shape and could be approximately fitted with a two-state Boltzmann function. Fig. 1 *C* and *D* shows representative gating current traces and their analyses for the V236F mutant.

To characterize the gating pore mutants, we compared the maximum τ values obtained from the activation and deactivation τ–*V* curves, respectively termed T^A and T^D, and the midpoint voltage obtained from the fitted *Q*–*V* curve, termed $V_{1/2}$. This analysis is graphically illustrated in Fig. 1*D*. These three gating parameters were determined for the other tested V236 mutants and plotted as a function of the mutated side chain, sorted from left to right by increasing $V_{1/2}$ values (Fig. 1*E*). Similar plots were made for the other gating pore residues tested, including I241 mutants whose *Q*–*V* curves, but not τ–*V* curves, were previously characterized (Table 1 and Fig. 2) (47). Because most F290 mutants were previously reported and because they display bisigmoid *Q*–*V* curves that cannot be fitted by a two-state Boltzmann

Table 1. Map of gating pore mutations

Position	G	A	S	T	C	V	L	I	M	P	F	Y	W	D	E	N	Q	H	K	R
V236	+	+	+	+	+	*	+	+	+	+	+	+	+			+	+			
I237	+	+	+	+	+	+	+	*	+	+	–	–	–	+	–	+	+	–	+	–
S240	+	+	*	+	+	+	–	–	+	–	+	+	+	+	–	+	+	+	–	–
I241	•	•	•	•	•	•	•	*	•		•	•	•	•		•	•	H$^+$		
F244	+	+	+	+	+	+	+	+	+		*	+	••			+	+	+		
C286	+	+	+	+	*	+	+	+	+	+	+	+	–			+	+			
I287	+	+	+	••	••	••	+	*	+		+	+	+	+		••	••	H$^+$		
F290	••	••	••	••		••	••	••	••		*	••	••			••	••			
A319		*	+	+	+	+	+	+	+	+	+	+	+			+	+			
I320	+	+	+	+	+	+	+	*	–		+	+				+	+	–		

The table shows new functional mutants analyzed in this study (+), mutants that were partially (•) or fully characterized (••) in previous studies, nontested mutants (blanks), nonfunctional mutants (–), and mutants previously shown to permeate protons at hyperpolarized voltages (H^+). In each row, the asterisk (*) indicates the native residue.

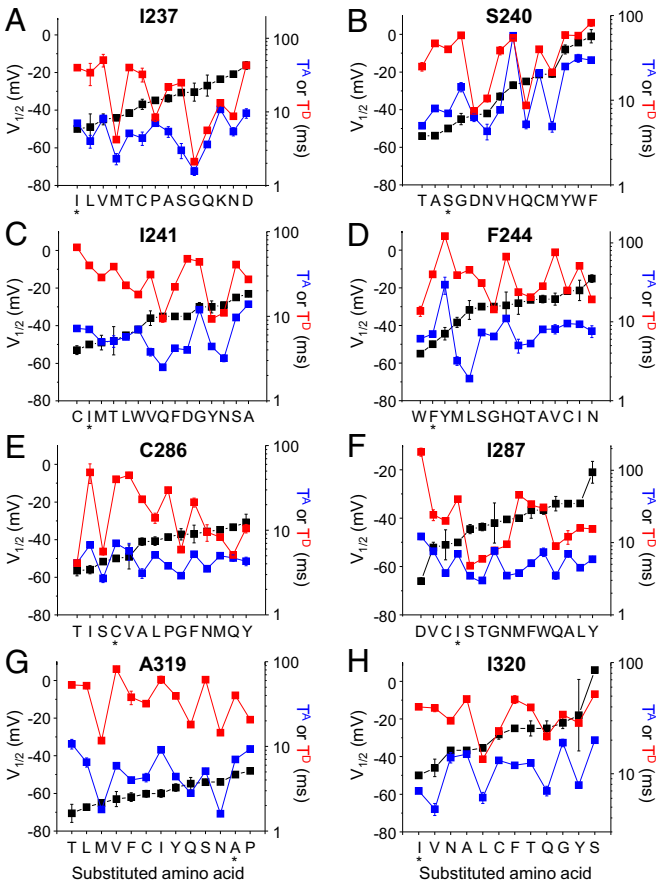

Fig. 2. Gating parameters of gating pore mutants. The observable gating parameters T^A (blue squares), T^D (red squares), and $V_{1/2}$ (black squares) as a function of the side chain present at position (*A*) I237, (*B*) S240, (*C*) I241, (*D*) F244, (*E*) C286, (*F*) I287, (*G*) A319, and (*H*) I320. The abscissa in each panel indicates the substituted amino acids, ordered according to a monotonic increase of the $V_{1/2}$ value. The $V_{1/2}$ values for the I241 mutants were obtained from ref. 47. For each position, the native residue is indicated by an asterisk.

function (38), their gating parameters are not shown in Fig. 2. Nevertheless, a refined interpretation of the role of F290 in VSD gating is provided in this study.

Mutating Most Gating Pore Residues Tends to Destabilize the Active vs. Resting State. Mutating the gating pore residues generally produced dramatic alterations of the kinetics and voltage dependence of the VSD (Fig. 2). A careful examination of Fig. 2 reveals that most gating pore mutations positively shift the VSD voltage dependence and accelerate its deactivation kinetics. This suggests that a major function of the endogenous gating pore residues is to bias the VSD thermodynamic equilibrium in favor of the active vs. the resting conformation. In vivo, opening of Kv channels leads to membrane repolarizations and consequently inhibits activated channels via a negative-feedback loop. The thermodynamic bias toward the activated conformation, provided by the native repertoire of gating pore residues, may thus help to delay this negative feedback by (*i*) slowing down pore closure and (*ii*) shifting the voltage sensitivity toward more negative voltages, providing neurons with more outward K^+ ion flux to repolarize their membranes more efficiently during the falling phase of the action potential.

Besides these effects, A319 is the only residue for which nearly all mutations yielded moderate negative *Q–V* shifts, up to −20 mV (Fig. 2*G*). Because A319 directly flanks S4 (Fig. 1*A*), A319 mutations may create steric hindrances that impede the repolarization-induced downward motion of the S4 helix and/or thermodynamically stabilize the active vs. resting state.

VSD Parameters Correlate with Physicochemical Properties of Gating Pore Residues. We systematically tested the presence of correlations between the VSD gating parameters ($V_{1/2}$, T^A, and T^D) and the amino acids' physicochemical parameters using a pairwise Pearson's linear correlation analysis (*Materials and Methods*) (Table 2). We tested four hydrophobicity scales: Kyte–Doolittle (KD) (54), Hessa–Hejne (HH) (55), Wimley–White (WW) (56), and Moon–Fleming (MF), as well as the van der Waals (vdW) surface area (57) or volume (58) of the substituted amino acid. For consistency among correlation tests, the MF and HH scales were inverted so that for all scales, more positive values indicate more hydrophobic residues. By calculating the corresponding *P* values for each test, we identified several levels of significance ranging from moderately significant ($*0.01 \le P < 0.05$) to highly significant ($***P < 0.001$) (Table 2).

This analysis led us to identify three groups among the gating pore residues. The first one does not display any significant correlation (A319 only). In this case, the interpretation of the role of A319 solely regarding our data are difficult because the absence of correlation does not allow us to discriminate between the possibilities that (*i*) neither the size nor hydrophobicity of

Table 2. Correlation analysis of gating pore residues

Position		WW	KD	HH	MF	SA	Vol
V236	$V_{1/2}$	−0.04	0.02	−0.11	0.26	−0.05	−0.16
	T^A	−0.04	0.52	0.44	0.16	0.05	0.23
	T^D	0.30	0.62*	0.59*	0.34	0.21	0.38
I237	$V_{1/2}$	−0.86***	−0.89***	−0.89***	−0.83***	−0.15	−0.29
	T^A	−0.62*	−0.22	−0.45	−0.26	0.14	0.38
	T^D	0.13	0.48	0.33	0.28	−0.28	0.12
S240	$V_{1/2}$	0.68*	0.18	0.27	0.51	0.90***	0.85***
	T^A	0.24	−0.09	0.03	−0.06	0.54*	0.45
	T^D	0.64	0.44	0.58	0.53	0.44	0.23
I241	$V_{1/2}$	−0.23	−0.44	−0.40	−0.33	−0.26	−0.38
	T^A	0.05	0.22	0.29	0.06	−0.44	−0.58*
	T^D	−0.31	0.26	0.08	−0.10	−0.51	−0.54*
F244	$V_{1/2}$	−0.79***	−0.01	−0.23	−0.46	−0.78**	−0.64*
	T^A	0.16	−0.20	−0.11	0.08	0.26	0.21
	T^D	0.08	0.13	0.11	0.28	0.29	0.39
C286	$V_{1/2}$	0.13	−0.43	−0.42	0.00	0.52	0.24
	T^A	0.38	0.63*	0.53	0.45	0.39	0.55
	T^D	0.12	0.66*	0.43	0.53	−0.11	0.11
I287	$V_{1/2}$	0.55*	−0.04	0.28	0.32	0.44	0.36
	T^A	0.39	0.41	0.44	0.48	0.25	0.05
	T^D	0.50	0.59*	0.61*	0.71**	0.54*	0.59*
F290	V_2	−0.79***	−0.11	−0.35	−0.47	−0.65*	−0.57*
	T^A	−0.07	−0.32	−0.42	−0.20	0.31	0.35
	T^D	0.84***	−0.19	0.03	0.24	0.78***	0.69**
A319	$V_{1/2}$	0.24	−0.46	−0.41	−0.10	0.20	0.13
	T^A	−0.05	0.24	0.18	0.31	−0.28	−0.18
	T^D	0.21	0.54	0.57	0.27	−0.10	0.01
I320	$V_{1/2}$	0.03	−0.50	−0.35	−0.33	−0.09	−0.26
	T^A	−0.24	−0.36	−0.24	−0.48	−0.61	−0.78*
	T^D	−0.01	0.12	0.18	0.06	−0.35	−0.30

The table indicates the Pearson pairwise correlation coefficient between each measured gating parameter (T^A, T^D, and $V_{1/2}$) and each tested side-chain physicochemical parameter: HH, KD, WW, MF, vdW surface area (SA), and volume (Vol), for each gating pore residue. The MF and HH scales were inverted such that more positive values indicate more hydrophobic residues in all hydrophobicity scales. The F290 mutants display bisigmoid *Q–V* curves; hence the second component V_2 is used instead of $V_{1/2}$ (*Results and Discussion*). The number of asterisks indicates the statistical significance as follows: $*0.01 \le P < 0.05$, $**0.001 \le P < 0.01$, and $***P < 0.001$.

A319 are important, or (*ii*) both the size and hydrophobicity are important, which would not be necessarily detected using a pairwise statistical test. The second group displays few moderately significant correlations (V236, I241, C286, and 320) with either the lateral chains' hydrophobicity or size. Finally, the third group displays one or more highly significant correlations (I237, S240, F244, I287, and F290). Hence, this last group will be the main focus of this paper.

The Hydrophobicity of I237 Controls the Voltage Dependence of Charge Movement. The I237 mutants exhibit highly significant correlations between the position of the *Q–V* curve on the voltage axis and every tested hydrophobicity scale, but not with the side-chain surface area or volume (Table 2). Fig. 3*A* shows the *Q–V* curves for each of the 13 mutants tested at position I237. Hydrophilic substitutions consistently shifted the *Q–V* curve toward more positive voltages, up to +40 mV for the I237D mutation. The midpoint $V_{1/2}$ values obtained for every tested amino acid present at position I237 were plotted against all four hydrophobicity scales (Fig. 3*B* and Fig. S2). A linear regression analysis of these plots reveals in each case a near-linear dependence between the hydrophobicity of the side chain at position I237 and the VSD voltage dependence ($0.66 < R^2 < 0.78$).

When plotting the $V_{1/2}$ against the vdW surface area or volume of the substituted amino acid, we observed two groups of mutants (Fig. 3 *C* and *D*). One group, formed by hydrophobic and moderately polar (Gly, Pro, Ser, and Thr) residues exhibits a linear correlation between $V_{1/2}$ and the side chain's surface or volume. This suggests that the channel's $V_{1/2}$ value is sensitive to the side-chain size at position I237; the larger the residue, the more stable the active state relative to the resting state (more negative $V_{1/2}$ values). However, when considering substitutions with Asp, Asn, Gln, and Lys, the strong polar nature of these residues seems to overcome the influence of the size, and the overall correlation between $V_{1/2}$ and size becomes insignificant. It is possible that these strong polar groups help to stabilize water molecules in the intracellular side of the gating pore, possibly enhancing hindrances preventing the passage of the gating charge during activation. We may rule out the creation of charge-specific salt bridges with the positive groups of the S4 Arg because substitutions with Lys or Asp produce similar effects (Fig. 3 *A–D*).

The interpretation of these results using a hypothetical two-state energy diagram is difficult because no significant correlation was observed between the side-chain hydrophobicity and VSD kinetics. However, I237 mutants generally exhibit faster deactivation kinetics (Fig. 2*A*, red squares). We may then speculate that the native Ile residue at position 237 helps to stabilize the active conformation, perhaps by creating an intracellular hydrophobic barrier that would oppose the return of the VSD charged groups. Interestingly, in the homologous VSD from the *Ciona intestinalis* voltage-sensitive phosphatase, a large side chain at position I126 (homologous to I237 in Shaker), was found important for normal VSD function (59). This difference highlights fundamental divergences in the gating mechanism between voltage-dependent ion channels and phosphatases.

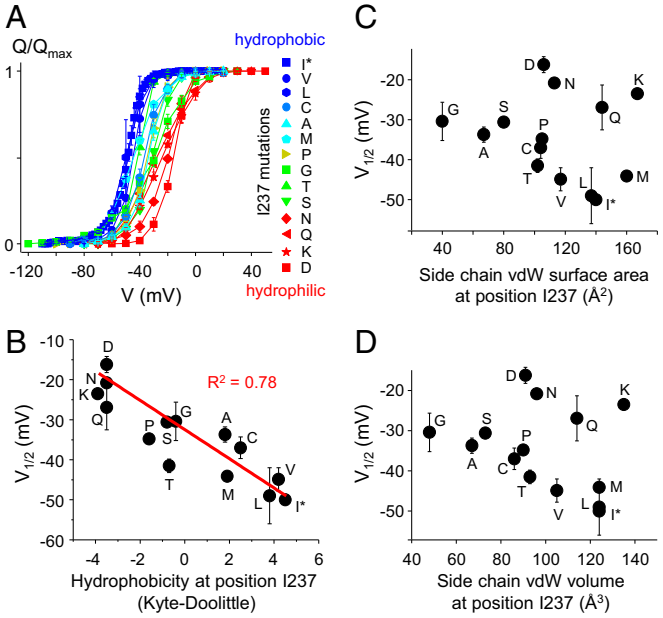

Fig. 3. Gating charge movement requires a hydrophobic residue at position I237. (*A*) *Q–V* curves for the I237 mutants colored from red to blue as the hydrophobicity of the substituted side chain increases. (*B*) The mean $V_{1/2}$ values obtained from each *Q–V* curve are plotted as a function of the hydrophobicity of the substituted side chain at position I237, using the KD hydrophobicity scale. These data are also plotted vs. other hydrophobicity scales (HH, WW, and MF) in Fig. S2. The R^2 value indicates the goodness of a linear fit to the data (red line), and letters indicate the substituted amino acid. (*C* and *D*) The mean $V_{1/2}$ values are plotted as a function of side chain vdW surface area (*C*) or volume (*D*). In all panels, the asterisk (*) indicates the native amino acid.

Large Substitutions at Position S240 Impede the Gating Charge Movement. The Kv1.2 refined X-ray structure shows that the residue homologous to S240 faces the tip of the side chain of R4 in the depolarized conformation (Fig. 1*A*) (21). S240 is the only gating pore residue capable of participating in hydrogen bond interactions and is well conserved in the VSD among Kv channels. An acidic Asp residue homologous to S240 controls ionic selectivity in voltage-gated proton channels (60) such as Hv1 (Fig. 1*B*). These observations thus argue that the hydroxyl group of S240 may assist VSD function, for instance by creating transient hydrogen bonds with the guanidinium groups of the S4 Arg. However, removing the hydroxyl group of S240 by substituting Ser for Ala did not appreciably alter the *Q–V* and τ–*V* curves nor the conductance (*G*) vs. voltage (*G–V*) curve, the latter measured from a conducting version of the S240A mutant (Fig. 4 *A–D*).

If the hydroxyl group of S240 is not required for normal VSD function, what could be the role of this residue? The VSD voltage dependence is extremely affected by the S240 mutations, shifting up to +60 mV for aromatic substitutions (Fig. 4*E*). Interestingly, $V_{1/2}$ is strongly correlated with the surface area (corr = +0.90; $R^2 = 0.85$) and volume (corr = +0.85; $R^2 = 0.83$) of the side chain at this position, being positively shifted as the size of the substituted side chain increases; these correlations are highly significant ($P < 0.001$) (Fig. 4*F* and Table 2). Increasing the size of the amino acid present at position S240 also tends to slow down activation kinetics (Fig. 2*B*, blue squares, and Table 2), suggesting that larger side chains stabilize the VSD resting state. These observations would place R1 at or below the level of S240 in the resting state, in agreement with previous studies (17, 61). Hence, the gap created by this conserved Ser residue may facilitate the sliding motion of the guanidinium groups by decreasing direct steric hindrances in the gating charge pathway.

Large Side Chains at Positions F244 and F290 Stabilize the Depolarized VSD Conformation. The phenylalanines present at positions F244 and F290 are important for the function of the Shaker channel, but their roles remain unclear (14, 38, 47, 62). Although a highly significant correlation ($P < 0.001$) exists between $V_{1/2}$ and WW for F244, no significant correlations were found with the other hydrophobicity scales, thus questioning the fundamental importance of F244 hydrophobicity (Table 2). However, significant correlations were also observed with both the surface area and

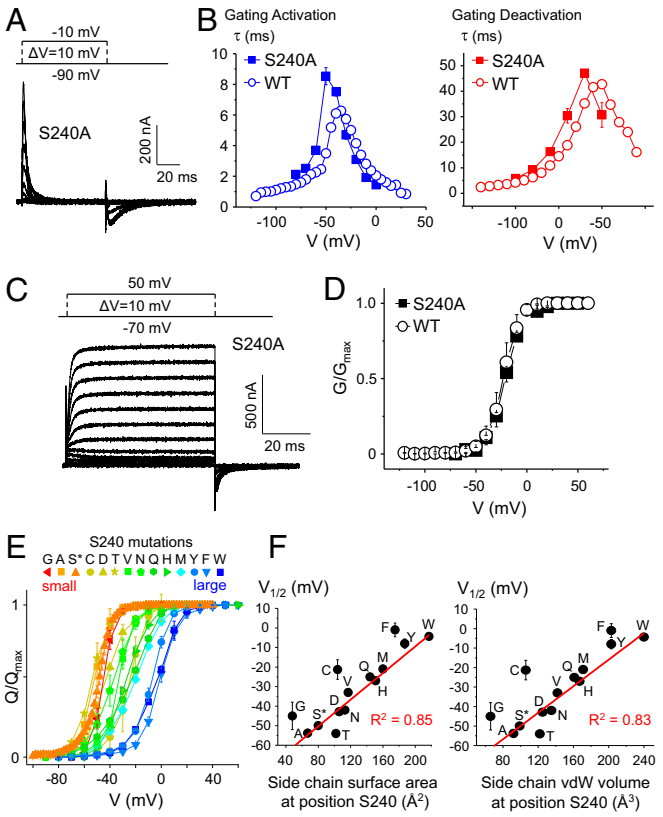

Fig. 4. VSD activation requires a small side chain, not a hydrophilic group, at position S240. (*A*) Gating current recordings for the S240A mutant. (*B*) τ–*V* plots showing the activation (blue) and deactivation (red) gating current weighted time constants (τ) as a function of the voltage pulse for the WT Shaker (open circles) and the S240A mutant (full squares). (*C*) Family of ionic current recordings measured in the conducting S240A mutant. (*D*) *G*–*V* curves for the WT Shaker (open circles) and the S240A mutant (full squares). (*E*) *Q*–*V* curves for the S240 mutants colored from red to blue as the size of the substituted side chain increases. (*F*) The mean $V_{1/2}$ values obtained from each *Q*–*V* curve are plotted as a function of the vdW surface area (*Left*) or volume (*Right*) of the substituted side chain at position S240. The R^2 values indicate the goodness of a linear fit to the data (red lines). Letters indicate substituted amino acids, and the asterisk indicates the native amino acid.

volume such that decreasing the size of the side chain present at position F244 displaces the $V_{1/2}$ toward positive voltages and speeds up deactivation kinetics (Fig. 5 *A* and *B*, and Table 2).

Could these steric effects at position F244 be mechanistically related? A simple hypothesis can explain both effects: the large residue F244 imparts a negative voltage dependence ($V_{1/2} \sim -50$ mV) and slow deactivation kinetics ($T^D \sim 40$ ms) to WT Shaker by stabilizing the activated state of the VSD (Fig. 5*C*, black continuous line). Decreasing the size of the side chain occupying this position, for instance with the F244A mutation, would destabilize the active vs. resting state (red dotted line). In this hypothesis, the consequences of the F244A mutation are (*i*) a reduction of the energy barrier rate-limiting for deactivation, which speeds up deactivation kinetics, and (*ii*) a bias of the thermodynamic equilibrium between the resting and active states, which positively shifts the *Q*–*V* curve.

Fig. 5*D* shows the *Q*–*V* curve of the F290A mutant taken from a previous study (38) to illustrate the unique phenotype of F290 mutations. The F290A mutation divides the *Q*–*V* curve into two unequal charge components with voltage midpoints of V_1 (~80% of total charge) and V_2 (~20% of total charge). This observation is not compatible with the "gating charge transfer center" hypothesis (62). Indeed, this hypothesis tells us that each gating charge (i.e., R1 to R4) must flip through a cyclic side chain (F290 in Shaker, F233 in Kv1.2) to be transported across the gating pore. This hypothesis mainly originated from conductance recordings of F290 mutants in Shaker channels (62). However, because in the Shaker channel pore opening is strictly coupled to a late concerted gating charge transition, conductance measurements do not inform on the bulk of the charge movement (63). Gating charge measurements of F290 mutants later revealed that, in contrast, none of the 13 tested F290 mutants affect the voltage dependence or kinetics of the bulk of gating charge movement (38). In fact, the F290 mutations only alter the late gating charge component associated with pore opening. Hence, the gating charge transfer hypothesis does not constitute a satisfying model to explain the role of this conserved Phe residue.

Although in the F290 mutants, the voltage dependence of the V_2 component and the T^D values were initially shown to correlate with the WW hydrophobicity (38), no significant correlations

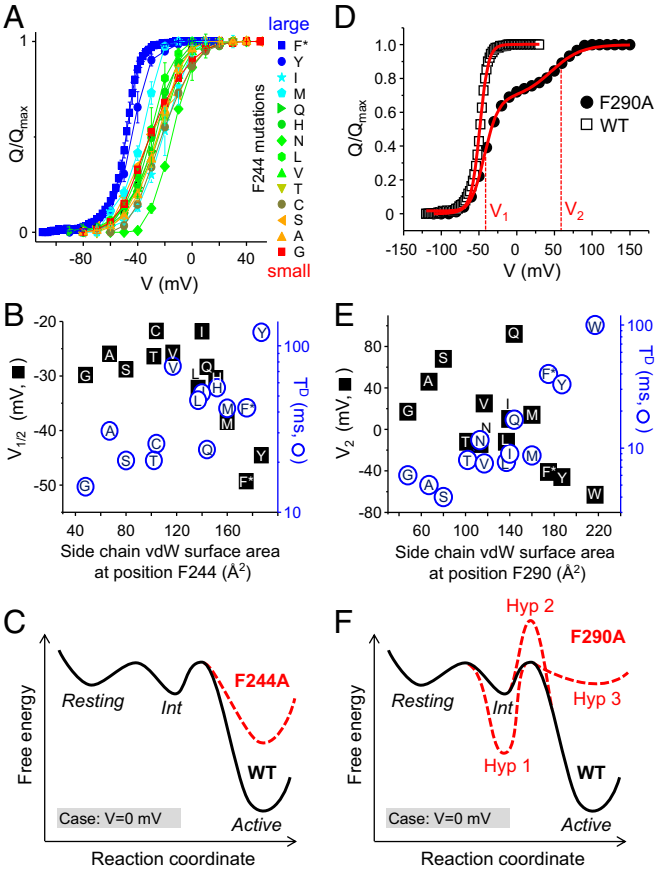

Fig. 5. Large side chains at positions F244 and F290 stabilize the activated state of the VSD. (*A*) *Q*–*V* curves for the F244 mutants colored from red to blue as the size of the substituted side chain increases. (*B*) Plots showing the mean $V_{1/2}$ (black squares) and T^D (blue circles) values as a function of the surface area of the substituted side chain at position F244. Letters indicate the substituted amino acid. (*C*) Hypothetical three-state energy landscape ($V = 0$ mV) illustrating the effect of the F244A mutation (red dotted line) relative to the WT channel (black line). (*D*) *Q*–*V* curves for the WT Shaker (black squares) and the F290A mutant (red circles) taken from a previous study (38). The *Q*–*V* curve for the F290A displays two components with distinct midpoint voltages V_1 and V_2. (*E*) The mean V_2 values (black squares) and T^D values (blue circles) plotted as a function of the surface area of the substituted side chain at position F290. (*F*) The hypothetical three-state energy landscape ($V = 0$ mV) for WT (black line) is shown with three alterations (Hyp-1 to -3, red dotted lines), which could explain the split of the *Q*–*V* curve imparted by the F290A mutation (see text).

were further found with the other three hydrophobicity scales (Table 2). However, similar to F244, V_2 and T^D have significant correlation with the size (surface area or volume) of substituted amino acids at position F290 (Table 2). Fig. 5*E* shows that increasing the surface area of the side chain present at position F290 displaces the isolated gating component V_2 back to negative voltages (black squares) and slows down deactivation (blue circles). These effects are similar to those observed for the F244 mutants, albeit in the case of the F290 mutants only the V_2 component is affected instead of the entire Q–V curve. This role of the side-chain size at position F290 is nicely consistent with the fact that the size of nonnatural Phe derivatives inserted at position F290 negatively correlated with the midpoint voltage of the channel's ionic conductance (62).

Can the complex phenotype of the F290 mutants be explained by a mechanism similar to the F244 case? Three simple mechanistic hypotheses may explain how decreasing the size of the side chain at position F290 increases the separation of the two gating charge components along the voltage axis (47, 63). First, small substitutions such as the F290A mutation could stabilize an intermediate state near the active state (Fig. 5*F*, "Int"), thus displacing the late gating component toward more depolarized voltages (Fig. 5*F*, "Hyp 1"). Second, these mutations may increase the energy barrier underlying the transition between P and active states ("Hyp 2"). This would slow down both activation and deactivation kinetics during this transition, thus making it difficult to resolve corresponding gating currents above electrical noise and hence produce an apparent Q–V split. Third, the mutations could destabilize the active state, forcing the VSD to transiently retreat to the intermediate state ("Hyp 3").

All these hypotheses predict that full VSD activation leading to pore opening requires much stronger depolarization, as is observed experimentally. However, only the last hypothesis predicts the experimentally observed acceleration of deactivation VSD kinetics as the Q–V split becomes more pronounced (Fig. 5*E*). Indeed, the first hypothesis predicts no significant changes in T^D because the deactivation energy barrier is unaffected. The second hypothesis predicts a slowing, not an acceleration, of both T^A and T^D. The third hypothesis predicts a diminution of the deactivation energy barrier, not because of a reduction in the peak between the P and active states as previously suggested (64), but because of an increase of the valley corresponding to the active state Gibbs free energy (Fig. 5*F*). Therefore, similar to F244 we propose that a large side chain is important at position F290 to stabilize the VSD active conformation.

How could large side chains stabilize the active state? In the refined X-ray structure of the depolarized Kv1.2 VSD (21), F244 and F290 flank R3 and R4, respectively (Fig. 1*A*). It is thus possible that the large surface area of these phenyl rings promotes van der Waals interactions at the interface of R3/F244 and R4/F290 in the depolarized VSD conformation. By holding S4 in its activated state, these Phe residues may physically act as "molecular clamps."

The I287D Mutation Immobilizes the VSD Depolarized State. Previous mutational analysis of I287 showed that the side-chain hydrophobicity at this position affects VSD kinetics (46). Our present correlation analysis, made on a slightly larger number of mutations, reveals that both hydrophobicity and size matter at position I287 (Table 2), suggesting that both chemical aspects of this lateral chain are important for VSD function. We also noticed that the T^D value of the I287D mutant was unusually slow (Fig. 2*F*). This was surprising because hydrophilic mutations at position I287 were expected to speed up VSD kinetics (46). Intriguingly, whereas the gating currents generated in the I287D channel during depolarization (ON-pulse) appear normal, the gating currents produced during repolarization (OFF-pulse) seem to progressively disappear as the amplitude of the depolarizing ON-pulse increases (Fig. 6*A*, *Right*). However, the repolarizing (deactivation) gating currents resurge upon stronger hyperpolarizing OFF-pulses (Fig. 6*B*). A conductive version of the I287D mutant channel is able to elicit normal outward K^+ currents but exhibits extremely slow pore closure kinetics (Fig. 6*C*, slow decaying OFF-pulse currents). These results show that (*i*) the I287D mutation immobilizes the VSD in the active conformation only and (*ii*) this immobilization is reversed upon strong hyperpolarization.

A possible underlying mechanism for these effects is that the negative charge carried by Asp at position I287 may create a salt bridge with one (or several) S4 Arg as the VSD reaches its activated conformation. To investigate this possibility, we sought to break these putative bridges by individually comutating the S4 Arg for Lys in the I287D channel. Indeed, isoelectric mutations are generally expected to alter intraprotein salt bridges because these interactions are extremely sensitive to the nature of the side chains and the spatial distribution of their electrical charges (65). Furthermore, isoelectric substitutions of R1–R3 maintain normal VSD function, facilitating phenotypic interpretations (47,

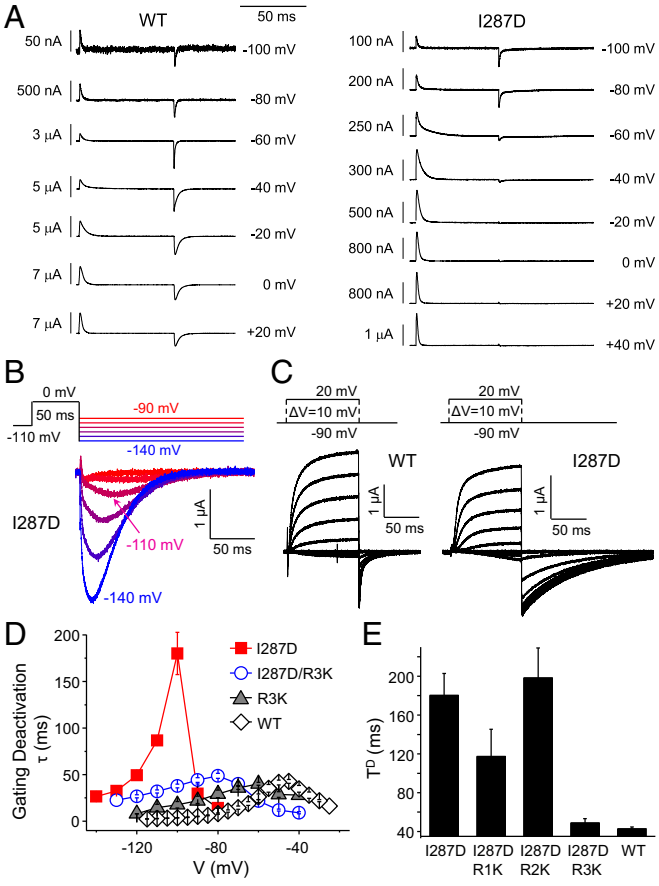

Fig. 6. I287D interacts with R3 in the depolarized state of the VSD. (*A*) Activation gating current traces are shown for WT (*Left*) and the I287D mutant (*Right*) for the indicated test pulse voltages (HP = −120 mV). Note the apparent immobilization of the gating charge during repolarization for the I287D mutant upon more positive test pulses. (*B*) Deactivation gating current traces shown for the I287D mutant as a function of the repolarizing pulse voltage. (*C*) Activation ionic current traces for the conductive WT Shaker and the I287D mutant (recorded at a temperature of 14 °C to better resolve pore closure). (*D*) Deactivation τ–V curves for WT (open diamonds), I287D (full squares), R3K (full triangles), and I287D/R3K (open circles). (*E*) Histogram showing the T^D values for WT Shaker and the indicated mutants.

66). Interestingly, the extreme slowing down of VSD deactivation imparted by the I287D mutation persists in presence of the additional mutation R1K or R2K, but not R3K, the latter comutation producing nearly WT-like deactivation kinetics (Fig. 6 *D* and *E*). These results suggest that I287D interacts with R3 in the active state of the VSD. Because no gating current could be detected in the double mutant I287D-R4K, the occurrence of interactions between I287D and R4 cannot be excluded. I287 was previously shown to lie within atomic proximity of R1 in the resting state, to seal the gating pore from ionic leak and to fine-tune the kinetic differences between Kv and Nav channels' VSDs, further supporting the importance of I287 to control the VSD activation energy barrier (17, 46).

Global Kinetics Modeling. It came to our attention that some correlations may have been missed in our approach because the reductionist parameters $V_{1/2}$, T^A, and T^D do not contain information on the steepness of the Q–V curves nor on the bell shape of the τ–V curves, which could both be altered by the gating pore mutations. Hence, we sought to simultaneously fit the Q–V and τ–V curves of all functional gating pore mutants (reported in this and previous studies except F290 mutants; Table 1) with the 2×2-state kinetic model described in Fig. 7. As in WT Shaker, the T^D values in most mutants are slower than the T^A values (Figs. 1*E* and 2), suggesting that most mutations lead to the normal stabilization of the channel's open state, with correspondingly slower deactivation kinetics (53, 67). To account for this effect, activation and deactivation are modeled as separate pathways (Fig. 7*A*, blue and red transitions) connected by the equilibrium constants $K_1 = k_{1f}/k_{1b}$ and $K_2 = k_{2f}/k_{2b}$, in which the states A2 and R1 are thermodynamically favored with respect to the states A1 and R2, respectively (Fig. 7*A*, thick black arrows). This assumption translates into the constraints $k_{1f} < k_{1b}$ and $k_{2f} > k_{2b}$ (equivalently $K_1 < 1$ and $K_2 > 1$). The model was further constrained by application of microscopic reversibility. This approach allowed us to globally fit each three-curve dataset with a minimal set of only six variable model parameters (a_{10}, z_{1f}, b_{10}, z_{1b}, b_{20}, z_{2b}). Details on the modeling can be found in *SI Text*, *Kinetic Modeling*, and Figs. S3–S5.

We next tested the presence of correlations between globally fit model parameters and the volume, surface area, or hydrophobicity of the side chain substituted at each position in the gating pore region. For correlation analysis, the observable gating parameters T^{A*}, T^{D*}, and $V_{1/2}{}^*$ were derived from the model fit, denoted by the asterisk. The heat map displayed in Fig. 8 indicates the statistical significance for all tested correlations, including the relationship type for significant correlations. Both red- and blue-colored boxes indicate the presence of significant correlations (red is positive; blue is negative), whereas gray boxes indicate no significant correlations. Consistent with our previous correlation analysis on the experimental parameters T^A, T^D, and $V_{1/2}$ (Table 2), the fitted parameters display significant, nearly exclusive correlations with either the size (S240, I241, F244) or hydrophobicity (I237) of the substituted side chain, whereas both the size and hydrophobicity are important physicochemical parameters for positions C286 and I287. This correlation analysis overall agrees with our previous analysis and thus validates our modeling approach.

The heat map shown in Fig. 8 may give precious clues to understand the relation between the chemical groups present in the gating pore and the fitted kinetic parameters describing the VSD movement with high accuracy. For instance, the highly significant negative correlation between $V_{1/2}{}^*$ and the side-chain hydrophobicity at position I237 (four consecutive dark blue boxes in panel I237 with values of $P < 0.001$) most likely originates from a positive correlation with the forward rate constant for the deactivation transition a_{20} (four consecutive red/dark red boxes in panel I237). Similarly, the positive correlation observed between

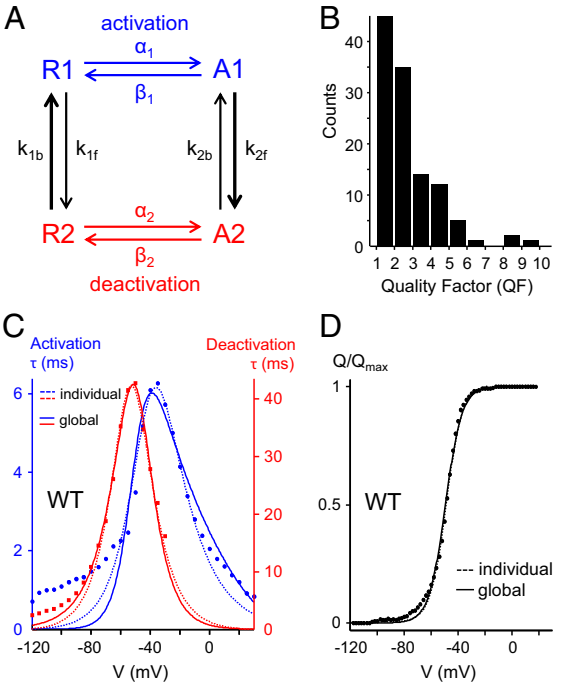

Fig. 7. Kinetic modeling. (*A*) Schematic representation of our 2×2-state kinetic model. Activation (blue) and deactivation (red) are produced in two parallel pathways to account for the slowing down of deactivation kinetics. (*B*) Distribution of global fit quality factor (QF) values for all tested mutants (*SI Text*). (*C*) Comparison of individual (dotted lines) and global fits (solid lines) for the activation (blue traces) and deactivation (red traces) τ–V curves obtained for WT Shaker. (*D*) Comparison of individual (dotted lines) and global fits (solid lines) of the Q–V curve obtained for WT Shaker.

T^{D*} and the side-chain size at position F244 is explained by a negative correlation with the deactivation rate constants b_{10} and b_{20}. In contrast, the negative correlation observed between T^{A*} and the residue surface area at position I241 seems to be caused by a negative correlation with z_{1f} and z_{2b}, the apparent valences for the forward activation and backward deactivation transitions, respectively. The molecular interpretation of a change of apparent valences is not straightforward because the fitted valences depend on both the total electrical charge moved and the number of intermediate states (47, 68). However, because (*i*) the gating pore mutations conserve the endogenous gating charge residues and (*ii*) the mutation I241W alters a VSD intermediate state (47), it is likely that steric effects at position I241 affect the energies of intermediate states. The situation is more complex for the correlation between $V_{1/2}{}^*$ and the side-chain size at position S240 because several correlations with multiple model parameters were observed (z_{2b}, a_{10}, a_{20}, b_{20}). These observations may constitute new avenues to understand the contribution of the gating pore to the bewildering diversity of functional modalities displayed by VSD-regulated proteins.

Our expansive set of mutations and model-based characterization allowed us to perform a detailed examination of the global effects of mutagenesis within a Kv channel's gating pore. Using model-derived values, Fig. S6 shows the distribution of mutational phenotypes for each of the observable gating parameters as a function of the mutated position or as a function of the substituted amino acid. Relative to the WT channel, the vast majority of mutations displace $V_{1/2}{}^*$ to more positive voltages (Fig. S6 *A* and *D*) and accelerate deactivation kinetics (Fig. S6 *C* and *F*). The scatter plots in Fig. S7 relate the observable gating parameters T^{A*} and T^{D*} to $V_{1/2}{}^*$ for all mutants tested. Using only point mutations, it is possible to finely tune the Shaker channel's gating

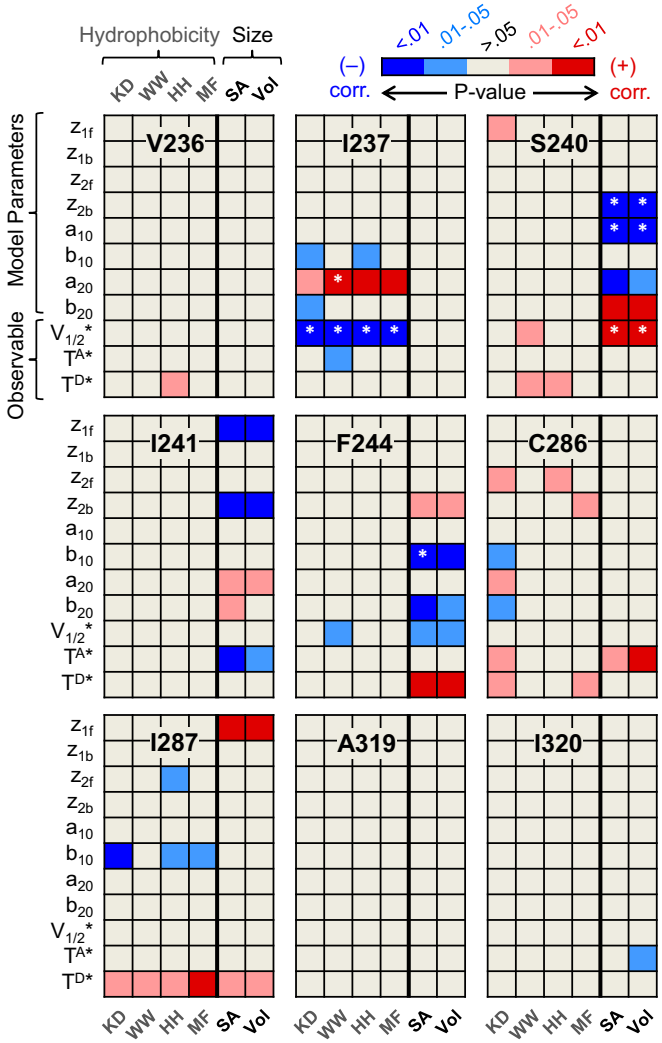

Fig. 8. Heat maps showing correlations between fitted gating parameters and side-chain physicochemical parameters. The maps show the color-coded *P* values obtained from Pearson pairwise correlation analysis between fitted gating parameters and the following: four hydrophobicity scales (KD, WW, HH, MF), the vdW surface area (SA), and the vdW volume (Vol) of the side chain present at the position of the indicated gating pore residue. For the observable gating parameters T^A*, T^D*, and $V_{1/2}$*, the asterisk denotes that these values were derived from the 2 × 2-state kinetic model global fit. Note that position 290 was excluded from such analysis due to the bisigmoidal nature of most of its mutants. The color code for correlation direction and *P* value range is at the top of the figure. The white asterisks denote highly significant correlations with $P < 0.001$.

parameters across nearly two orders of magnitude in both activation and deactivation kinetics, and at least a 70-mV range for *Q–V* voltage midpoint (Fig. S7). This result may be especially useful for engineered applications in which specific gating properties are desired.

Conclusions

Our main findings are summarized in Fig. 9. A steric gap at position S240 defines the primary entryway for the gating charges during activation, whereas both size and hydrophobicity of I287 are important to control the energy barrier underlying VSD kinetics (Fig. 9 *A* and *B*). The stabilization of the voltage sensor in its depolarized (active) conformation is strengthened by two phenyl rings at positions F244 and F290 that likely act as "molecular clamps," and by I237, which creates a localized hydrophobic barrier that prevents reentry of the gating charges into the gating pore (Fig. 9*C*). Our global kinetic analyses give clues to understand the relations between chemical groups present in the gating pore and the underlying kinetic parameters that describe the VSD movement.

Materials and Methods

Mutagenesis and Expression in *Xenopus* Oocytes. Mutations were introduced in cDNA encoding the N-inactivation removed, nonconducting W434F Shaker K^+ channel Δ4–46 using QuikChange mutagenesis (Stratagene) as described previously (69). All mutants were verified by sequencing the whole cDNA.

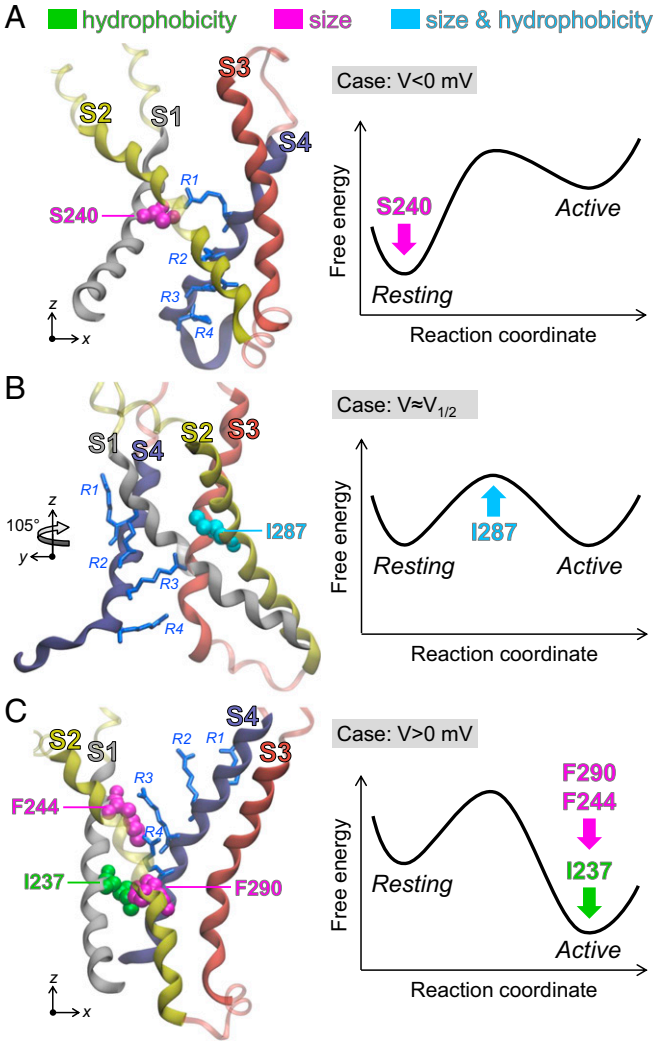

Fig. 9. Contributions of gating pore residues to the VSD energy landscape. (*A*) (*Left*) Position of R1 as it moves near S240 (magenta) in a resting-state cartoon model of the Kv1.2 VSD (47) (resting state, image 32, ref. 47). (*Right*) Simplified two-state energy diagram showing how increasing the size of the amino acid at position S240 (magenta arrow) prevents the passage of the gating charge, hence stabilizing the resting state relative to active state. (*B*) (*Left*) Intermediate-state cartoon model of the Kv1.2 VSD (47) (intermediate state, image 22, ref. 47) showing the positions of R1–R4 and I287. The VSD was rotated 105° about the *z* axis. (*Right*) Both size and hydrophobicity of I287 are important to control the VSD main energy barrier. (*C*) (*Left*) Active-state cartoon model of the Kv1.2 VSD (47) (active state, image 1, ref. 47) showing the positions of the S4 Arg, I237, F244, and F290. (*Right*) Increasing the size of the side chain at position F244 (magenta arrow) or increasing the hydrophobicity at position I237 (green arrow) stabilizes the active state. A diagrammatic representation of the role of F290 is shown in Fig. 5*F*.

cRNAs were produced using a T7 RNA expression kit (Ambion) and injected into *Xenopus laevis* oocytes. Injected oocytes were maintained in a standard oocyte solution containing 100 mM NaCl, 5 mM KCl, 2 mM $CaCl_2$, and 10 mM Hepes at pH 7.5, supplemented with 50 μg/mL gentamycin for 2–6 d at 16.5 °C.

Electrophysiology. Gating and ionic currents were recorded using the cut-open voltage-clamp method at room temperature, unless otherwise stated. The recording pipette resistance was 0.5–0.8 MΩ. Data were acquired at a sampling frequency of 30–100 kHz and filtered on-line at 5–20 kHz using a low-pass Bessel filter mounted in the amplifier (Dagan). Capacitive transient currents were subtracted on-line using the P/4 method when possible. In-house software was used for data collection (Gpatch) and analysis of currents (Analysis). For gating current recordings, the internal solution was 115 mM *N*-methyl-D-glucamine (NMG) methylsulfonate (Mes), 2 mM EGTA, and 10 mM Hepes, pH 7.5; the external solution was 115 mM NMG-Mes, 2 mM Ca-Mes, and 10 mM Hepes, pH 7.5. For ionic current recordings (Figs. 4 *C* and *D* and 6*C*), the internal solution was 115 mM K^+-Mes, 2 mM EGTA, and 10 mM Hepes, pH 7.5; the external solution was 10–50 mM K^+-Mes, 65–105 mM NMG-Mes, 2 mM Ca-Mes, and 10 mM Hepes, pH 7.5.

Data Analysis. The time constant (τ) of gating or ionic currents was determined by a least-squares fit of the whole decaying part of each trace, using a single- or double-exponential function as appropriate. When a double-exponential fit was used, an amplitude-weighted average time constant was calculated. All data curves (Q–V, τ–V, G–V) are representative of n = 4–8 independent experiments, with mean value calculated at each test voltage. Error bars represent the SEM. To determine midpoint voltages, Q–V curves were individually fitted by a simple two-state Boltzmann equation:

$$\frac{Q(V)}{Q_{max}} = \frac{1}{1+\exp\left[\frac{-ze_0(V-V_{1/2})}{kT}\right]}, \quad [1]$$

where z, e_0, $V_{1/2}$, k, and T are the valence (times the fraction of the electric field), electronic charge, voltage at which charge is equally distributed between states, Boltzmann constant, and absolute temperature, respectively. Mean $V_{1/2}$ values were obtained for each mutant by averaging $V_{1/2}$ values obtained from individual Q–V fits. Bisigmoidal Q–V curves related to Fig. 5*D* were fit by a sequential three-state model equation (47) as follows:

$$\frac{Q(V)}{Q_{max}} = \frac{z_2 + z_1\left(1+\exp\left[\frac{-z_2e_0(V-V_2)}{kT}\right]\right)}{1+\exp\left[\frac{-z_2e_0(V-V_2)}{kT}\right]\left(1+\exp\left[\frac{-z_1e_0(V-V_1)}{kT}\right]\right)}, \quad [2]$$

where subscripts denote the valence and voltage midpoint for the first and second state transitions, and other variables have the same meaning. All Q–V fits were performed in the least-squares sense on mean Q–V data curves. See also *SI Text* for a detailed procedure on fitting the 2 × 2-state kinetic model.

Correlation Analysis. Correlations were calculated using Pearson's linear correlation coefficient:

$$\mathrm{corr}(X,Y) = \frac{E\left[(X-\mu_X)(Y-\mu_Y)\right]}{S_X S_Y}, \quad [3]$$

where X and Y are pairwise random variables, μ is the sample mean, and s is the uncorrected sample SD. For all correlation calculations, model parameters and model-derived observable gating parameters were first transformed according to their approximate distribution: (z_{1f}, z_{1b}, z_{2f}, z_{2b}, $V_{1/2}$*) were left untransformed and (a_{10}, b_{10}, a_{20}, b_{20}, T^A*, T^D*) were log transformed. The P value was calculated using Student's t distribution for a transformation of the correlation, for testing the null hypothesis of no correlation against the alternative that there is a nonzero correlation (two-tailed test). Correlations were visually illustrated by a P value map in Fig. 8, in which the pixels of a 2D parameter grid are colored by the significance level range and correlation relationship (– or +). Due to the limited number of possible side-chain mutations, the sample size for such correlations was small (n = 10–15, $\langle n \rangle$ = 13.3).

ACKNOWLEDGMENTS. We thank Dr. Eduardo Perozo, Dr. Benoit Roux, Dr. Ramón Latorre, Dr. Tomoya Kubota, and Michael F. Priest for commenting on the manuscript. This work was supported by National Institutes of Health Grant GM030376.

1. El Chemaly A, Demaurex N (2012) Do Hv1 proton channels regulate the ionic and redox homeostasis of phagosomes? *Mol Cell Endocrinol* 353(1-2):82–87.
2. Murata Y, Iwasaki H, Sasaki M, Inaba K, Okamura Y (2005) Phosphoinositide phosphatase activity coupled to an intrinsic voltage sensor. *Nature* 435(7046):1239–1243.
3. Ben-Chaim Y, et al. (2006) Movement of "gating charge" is coupled to ligand binding in a G-protein-coupled receptor. *Nature* 444(7115):106–109.
4. Biel M, Wahl-Schott C, Michalakis S, Zong X (2009) Hyperpolarization-activated cation channels: From genes to function. *Physiol Rev* 89(3):847–885.
5. Hodgkin AL, Huxley AF (1952) A quantitative description of membrane current and its application to conduction and excitation in nerve. *J Physiol* 117(4):500–544.
6. Jensen MO, et al. (2012) Mechanism of voltage gating in potassium channels. *Science* 336(6078):229–233.
7. Jacobson DA, et al. (2010) Calcium-activated and voltage-gated potassium channels of the pancreatic islet impart distinct and complementary roles during secretagogue induced electrical responses. *J Physiol* 588(Pt 18):3525–3537.
8. Zhu X, Mose E, Zimmermann N (2013) Proton channel HVCN1 is required for effector functions of mouse eosinophils. *BMC Immunol* 14:24.
9. Long SB, Campbell EB, Mackinnon R (2005) Crystal structure of a mammalian voltage-dependent Shaker family K^+ channel. *Science* 309(5736):897–903.
10. Sasaki M, Takagi M, Okamura Y (2006) A voltage sensor-domain protein is a voltage-gated proton channel. *Science* 312(5773):589–592.
11. Ramsey IS, Moran MM, Chong JA, Clapham DE (2006) A voltage-gated proton-selective channel lacking the pore domain. *Nature* 440(7088):1213–1216.
12. Seoh SA, Sigg D, Papazian DM, Bezanilla F (1996) Voltage-sensing residues in the S2 and S4 segments of the Shaker K^+ channel. *Neuron* 16(6):1159–1167.
13. Aggarwal SK, MacKinnon R (1996) Contribution of the S4 segment to gating charge in the Shaker K^+ channel. *Neuron* 16(6):1169–1177.
14. Pless SA, Galpin JD, Niciforovic AP, Ahern CA (2011) Contributions of counter-charge in a potassium channel voltage-sensor domain. *Nat Chem Biol* 7(9):617–623.
15. Chanda B, Bezanilla F (2008) A common pathway for charge transport through voltage-sensing domains. *Neuron* 57(3):345–351.
16. Starace DM, Bezanilla F (2004) A proton pore in a potassium channel voltage sensor reveals a focused electric field. *Nature* 427(6974):548–553.
17. Campos FV, Chanda B, Roux B, Bezanilla F (2007) Two atomic constraints unambiguously position the S4 segment relative to S1 and S2 segments in the closed state of Shaker K channel. *Proc Natl Acad Sci USA* 104(19):7904–7909.
18. Ahern CA, Horn R (2005) Focused electric field across the voltage sensor of potassium channels. *Neuron* 48(1):25–29.
19. Asamoah OK, Wuskell JP, Loew LM, Bezanilla F (2003) A fluorometric approach to local electric field measurements in a voltage-gated ion channel. *Neuron* 37(1):85–97.
20. Islas LD, Sigworth FJ (2001) Electrostatics and the gating pore of Shaker potassium channels. *J Gen Physiol* 117(1):69–89.
21. Chen X, Wang Q, Ni F, Ma J (2010) Structure of the full-length Shaker potassium channel Kv1.2 by normal-mode-based X-ray crystallographic refinement. *Proc Natl Acad Sci USA* 107(25):11352–11357.
22. Chamberlin A, et al. (2014) Hydrophobic plug functions as a gate in voltage-gated proton channels. *Proc Natl Acad Sci USA* 111(2):E273–E282.
23. Long SB, Tao X, Campbell EB, MacKinnon R (2007) Atomic structure of a voltage-dependent K^+ channel in a lipid membrane-like environment. *Nature* 450(7168):376–382.
24. Khalili-Araghi F, et al. (2010) Calculation of the gating charge for the Kv1.2 voltage-activated potassium channel. *Biophys J* 98(10):2189–2198.
25. Delemotte L, Tarek M, Klein ML, Amaral C, Treptow W (2011) Intermediate states of the Kv1.2 voltage sensor from atomistic molecular dynamics simulations. *Proc Natl Acad Sci USA* 108(15):6109–6114.
26. Vargas E, Bezanilla F, Roux B (2011) In search of a consensus model of the resting state of a voltage-sensing domain. *Neuron* 72(5):713–720.
27. Vargas E, et al. (2012) An emerging consensus on voltage-dependent gating from computational modeling and molecular dynamics simulations. *J Gen Physiol* 140(6):587–594.
28. Imbrici P, D'Adamo MC, Kullmann DM, Pessia M (2006) Episodic ataxia type 1 mutations in the KCNA1 gene impair the fast inactivation properties of the human potassium channels Kv1.4-1.1/Kvbeta1.1 and Kv1.4-1.1/Kvbeta1.2. *Eur J Neurosci* 24(11):3073–3083.
29. Browne DL, et al. (1995) Identification of two new KCNA1 mutations in episodic ataxia/myokymia families. *Hum Mol Genet* 4(9):1671–1672.
30. Adelman JP, Bond CT, Pessia M, Maylie J (1995) Episodic ataxia results from voltage-dependent potassium channels with altered functions. *Neuron* 15(6):1449–1454.
31. Zhu J, Alsaber R, Zhao J, Ribeiro-Hurley E, Thornhill WB (2012) Characterization of the Kv1.1 I262T and S342I mutations associated with episodic ataxia 1 with distinct phenotypes. *Arch Biochem Biophys* 524(2):99–105.
32. Singh NA, et al. (2009) A role of SCN9A in human epilepsies, as a cause of febrile seizures and as a potential modifier of Dravet syndrome. *PLoS Genet* 5(9):e1000649.
33. Yang P, et al. (2002) Allelic variants in long-QT disease genes in patients with drug-associated torsades de pointes. *Circulation* 105(16):1943–1948.
34. Paulussen AD, et al. (2004) Genetic variations of KCNQ1, KCNH2, SCN5A, KCNE1, and KCNE2 in drug-induced long QT syndrome patients. *J Mol Med (Berl)* 82(3):182–188.
35. Fujiwara T, et al. (2003) Mutations of sodium channel alpha subunit type 1 (SCN1A) in intractable childhood epilepsies with frequent generalized tonic-clonic seizures. *Brain* 126(Pt 3):531–546.

36. Petitprez S, et al. (2008) A novel dominant mutation of the Nav1.4 alpha-subunit domain I leading to sodium channel myotonia. *Neurology* 71(21):1669–1675.
37. Kwong AK, Fung CW, Chan SY, Wong VC (2012) Identification of SCN1A and PCDH19 mutations in Chinese children with Dravet syndrome. *PLoS One* 7(7):e41802.
38. Lacroix JJ, Bezanilla F (2011) Control of a final gating charge transition by a hydrophobic residue in the S2 segment of a K^+ channel voltage sensor. *Proc Natl Acad Sci USA* 108(16):6444–6449.
39. Li-Smerin Y, Hackos DH, Swartz KJ (2000) alpha-helical structural elements within the voltage-sensing domains of a K^+ channel. *J Gen Physiol* 115(1):33–50.
40. Muroi Y, Arcisio-Miranda M, Chowdhury S, Chanda B (2010) Molecular determinants of coupling between the domain III voltage sensor and pore of a sodium channel. *Nat Struct Mol Biol* 17(2):230–237.
41. Soler-Llavina GJ, Chang TH, Swartz KJ (2006) Functional interactions at the interface between voltage-sensing and pore domains in the Shaker K(v) channel. *Neuron* 52(4): 623–634.
42. Hackos DH, Chang TH, Swartz KJ (2002) Scanning the intracellular S6 activation gate in the shaker K^+ channel. *J Gen Physiol* 119(6):521–532.
43. Li-Smerin Y, Hackos DH, Swartz KJ (2000) A localized interaction surface for voltage-sensing domains on the pore domain of a K^+ channel. *Neuron* 25(2):411–423.
44. Swartz KJ, MacKinnon R (1997) Mapping the receptor site for hanatoxin, a gating modifier of voltage-dependent K^+ channels. *Neuron* 18(4):675–682.
45. Yifrach O, MacKinnon R (2002) Energetics of pore opening in a voltage-gated K^+ channel. *Cell* 111(2):231–239.
46. Lacroix JJ, Campos FV, Frezza L, Bezanilla F (2013) Molecular bases for the asynchronous activation of sodium and potassium channels required for nerve impulse generation. *Neuron* 79(4):651–657.
47. Lacroix JJ, et al. (2012) Intermediate state trapping of a voltage sensor. *J Gen Physiol* 140(6):635–652.
48. Stefani E, Bezanilla F (1998) Cut-open oocyte voltage-clamp technique. *Methods Enzymol* 293:300–318.
49. Mathur R, Zhou J, Babila T, Koren G (1999) Ile-177 and Ser-180 in the S1 segment are critically important in Kv1.1 channel function. *J Biol Chem* 274(17):11487–11493.
50. Perozo E, MacKinnon R, Bezanilla F, Stefani E (1993) Gating currents from a nonconducting mutant reveal open-closed conformations in Shaker K^+ channels. *Neuron* 11(2):353–358.
51. Yang Y, Yan Y, Sigworth FJ (1997) How does the W434F mutation block current in Shaker potassium channels? *J Gen Physiol* 109(6):779–789.
52. Pless SA, Galpin JD, Niciforovic AP, Kurata HT, Ahern CA (2013) Hydrogen bonds as molecular timers for slow inactivation in voltage-gated potassium channels. *Elife* 2: e01289.
53. Lacroix JJ, Labro AJ, Bezanilla F (2011) Properties of deactivation gating currents in Shaker channels. *Biophys J* 100(5):L28–L30.
54. Kyte J, Doolittle RF (1982) A simple method for displaying the hydropathic character of a protein. *J Mol Biol* 157(1):105–132.
55. Hessa T, et al. (2005) Recognition of transmembrane helices by the endoplasmic reticulum translocon. *Nature* 433(7024):377–381.
56. Wimley WC, White SH (1996) Experimentally determined hydrophobicity scale for proteins at membrane interfaces. *Nat Struct Biol* 3(10):842–848.
57. Miller S, Janin J, Lesk AM, Chothia C (1987) Interior and surface of monomeric proteins. *J Mol Biol* 196(3):641–656.
58. Darby NJ, Creighton TE (1993) *Protein Structure* (Oxford Univ Press, Oxford).
59. Lacroix JJ, Bezanilla F (2012) Tuning the voltage-sensor motion with a single residue. *Biophys J* 103(3):L23–L25.
60. Musset B, et al. (2011) Aspartate 112 is the selectivity filter of the human voltage-gated proton channel. *Nature* 480(7376):273–277.
61. Lin MC, Hsieh JY, Mock AF, Papazian DM (2011) R1 in the Shaker S4 occupies the gating charge transfer center in the resting state. *J Gen Physiol* 138(2):155–163.
62. Tao X, Lee A, Limapichat W, Dougherty DA, MacKinnon R (2010) A gating charge transfer center in voltage sensors. *Science* 328(5974):67–73.
63. Ledwell JL, Aldrich RW (1999) Mutations in the S4 region isolate the final voltage-dependent cooperative step in potassium channel activation. *J Gen Physiol* 113(3): 389–414.
64. Schwaiger CS, Liin SI, Elinder F, Lindahl E (2013) The conserved phenylalanine in the K^+ channel voltage-sensor domain creates a barrier with unidirectional effects. *Biophys J* 104(1):75–84.
65. Donald JE, Kulp DW, DeGrado WF (2011) Salt bridges: Geometrically specific, designable interactions. *Proteins* 79(3):898–915.
66. Papazian DM, Timpe LC, Jan YN, Jan LY (1991) Alteration of voltage-dependence of Shaker potassium channel by mutations in the S4 sequence. *Nature* 349(6307):305–310.
67. Batulan Z, Haddad GA, Blunck R (2010) An intersubunit interaction between S4-S5 linker and S6 is responsible for the slow off-gating component in Shaker K^+ channels. *J Biol Chem* 285(18):14005–14019.
68. Bezanilla F, Villalba-Galea CA (2013) The gating charge should not be estimated by fitting a two-state model to a Q-V curve. *J Gen Physiol* 142(6):575–578.
69. Starace DM, Bezanilla F (2001) Histidine scanning mutagenesis of basic residues of the S4 segment of the shaker K^+ channel. *J Gen Physiol* 117(5):469–490.